Article

Hybrid boost-cuk converter with bat-chicken swarm-optimized PI controller for photovoltaic grid systems

S. Hema[1]*, S. Sreedevi[2], K. Harinath Reddy[3], Siddheswar Kar[4], Ananthan Nagarajan[5], S. Sengottaian[6]

[1]Department of Biomedical Engineering, Vel Tech Rangarajan Dr. Sagunthala R&D Institute of Science and Technology, Chennai-600062, India

[2]Department of Electrical and Electronics Engineering, Sriram Engineering College, Perumalpattu - 602 024, India

[3]Department of Electrical and Electronics Engineering, Annamacharya University, Rajampet, India

[4]Department of Electrical Engineering, Medi-Caps University, Indore, Madhya Pradesh, India

[5]Department of Electrical and Electronics Engineering, Vel Tech Multi Tech Dr. Rangarajan Dr. Sakunthala Engineering College, Chennai 62, India

[6]Department of Electrical and Electronics Engineering, Viswam Engineering College, Madanapalle-517 325, Andhra Pradesh

A R T I C L E   I N F O

A B S T R A C T

Recently, the reduction of greenhouse gas emissions and fuel consumption has been attended to by adopting the Photovoltaic (PV) system. Due to their intermittent nature, energy generated by PV systems is unpredictable for microgrid operation. Therefore, in this research, a novel hybrid Boost-Cuk converter is developed to efficiently increase the low voltage received from the PV system. Subsequently, the Bat-Chicken swarm optimized Proportional Integral (PI) controller is exploited to adjust the PI controller's parameters. Furthermore, the intermittency and instability of PV systems are addressed by adding a Battery Energy Storage System (BESS) to the microgrid to provide a steady and continuous power supply. This output is delivered to the grid via a Three Phase Voltage Source Inverter (3ϕ VSI), and the grid synchronization is accomplished with the aid of a PI controller. In order to validate the efficacy of the developed work, it is executed using the MATLAB/Simulink tool and compared with traditional topologies. The outcomes reveal that the developed research attains an efficacy of 93%, ensuring effective grid synchronization.

1. Introduction

More fossil fuels are used to produce power, which increases environmental pollution. In addition to being the primary source of electrical production worldwide, fossil fuels are the main contributors to environmental degradation [1]. To reduce the negative effects of using fossil fuels, renewable energy systems (RES) like solar, wind, biomass, and hydraulic energies have received much attention [2]. Clean energy, such as PV, has drawn more and more attention as the environmental pollution issues brought on by conventional fossil fuels become more noticeable [3-5]. Effectively converting solar into affordable power without wasting energy is the main goal of all PV systems. Due to its plentiful resources and pollution-free benefits, grid-tied PV power generation technology has experienced rapid expansion [6-7]. Large-scale PV power-generation networks' ongoing grid integration results in a decline in the system's short-circuit capacity, which lowers the voltage support capacity [8]. However, Energy Storage Systems (ESSs) have been installed to guarantee a reliable power supply due to the variable nature of PV production systems during the day and their unavailability at night [9-10]. Numerous meteorological factors, including solar radiation, temperature, wind speed, precipitation, humidity, dust deposition, air pressure, and technical factors like inverter loss and PV array losses, affect the performance of solar PV power stations [11-12].

Abbreviations	
AC	Alternating Current
BA	Bat Algorithm
BESS	Battery Energy Storage System
CN	Chick Group
CSO	Chicken Swarm Optimization
DC	Direct Current
ESS	Energy Storage System
G2V	Grid to Vehicle
HN	Hen Group
HS	Harmony Search
LPF	Low Pass Filter
PI	Proportional-Integral
PV	Photovoltaic
PWM	Pulse Width Modulation
QBC	Quadratic Boost Converter
RES	Renewable Energy System
RN	Rooster Group
SRF-PLL	Synchronous Reference Frame-Phase Locked Loop
V2G	Vehicle to Grid
VSI	Voltage Source Inverter

Since PV systems depend on ambient temperature and solar irradiance, their output power typically varies during the day [13, 14]. The Quadratic Boost Converter, which achieves high voltage gain with a single switch, is represented by S. Chitra Selvi et al. [15]. However, QBC's high-frequency switching results in better switching losses, which reduces the system's effectiveness. Ahmed et al. [16] presented an interleaved Boost Converter with high conversion efficiency and lower switching losses. However, this converter requires more components, enhancing the overall cost and complexity. A transformerless boost converter that achieves high voltage gain without requiring high-duty cycles is designed by Ahmed et al. [17]. However, its increased input current ripple impacts the associated load's performance. Haider et al. [18] presented the high-gain Cuk converter sustaining a smooth current waveform because of the capacitors and inductors at both input and output sides. However, the operation and implementation of this converter are complex, and dynamic operation leads to high current stress on switches.

A quadratic Cuk converter was developed by H. Gholizadeh et al. [19] that reduces electromagnetic interference by maintaining a stable input current with minimal ripple. Nevertheless, the converter is effective; there are some power losses because of the extra components and switching operations. Therefore, this paper uses a hybrid Boost-Cuk converter to enhance the low voltage of the PV system. The PI controller is exploited to manage the function of the hybrid Boost-Cuk converter, and its parameters are tuned by the optimization algorithm. In order to address nonlinear, non-differentiable, and multi-modal optimization issues, the particle swarm optimization approach was introduced by Demir et al. [20]. However, it cannot ensure that the best solution will be found, especially for extremely complicated or multi-modal issues. In Shamseldin et al. [21] research, a Harmony Search (HS) optimization algorithm is developed, which sustains a good balance between exploration and exploitation. Nevertheless, the performance of HS is significantly affected by the initial harmony memory, which leads to suboptimal solutions. The Cuckoo Search Optimization technique improves accuracy and efficiency in optimization tasks while exhibiting reasonable convergence rates. Nevertheless, the algorithm's effectiveness is reduced by the initial fixed parameters, necessitating improvements for improved performance [22]. In Amador-Angulo et al. [23], a Chicken search optimization algorithm is developed that has shown competitive performance on a wide range of benchmark problems. The computational cost is high for large and complex problems, limiting its practical applications. As a result, the Bat-Chicken swarm optimization algorithm is exploited to fine-tune the PI controller's parameters. The main motivations of this research are:

- Implementing the hybrid Boost-Cuk converter that effectively enhances the low output voltage of the PV system.
- The parameters of the PI controller are fine-tuned with the aid of the Bat-Chicken swarm optimization algorithm.
- The battery is exploited to store the surplus energy from the PV system, and a bidirectional DC-DC converter is implemented to perform the battery's charging and discharging operations.
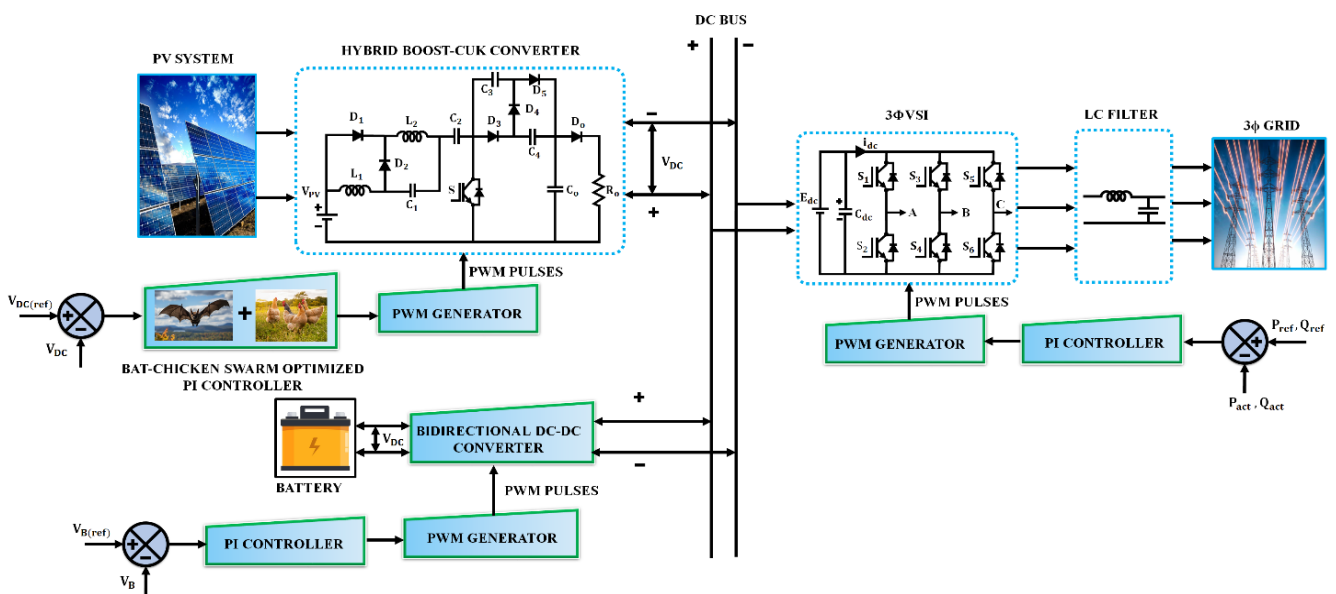
Figure 1. Block diagram of PV-based grid system

2. Proposed methodology

Figure 1 reveals the block diagram of the developed PV-based grid system. The PV system generates low voltage because of varying environmental conditions, which is boosted with the aid of a hybrid boost-Cuk converter. Nevertheless, the voltage of the developed converter, which is regulated by a PI controller, is unstable, and its parameters are tuned by a Bat-Chicken swarm optimization algorithm. After that, the Pulse Width Modulation (PWM) generator produces PWM pulses to better operate the developed converter. A Bidirectional DC-DC Converter enables charging and discharging operations, and battery voltage is regulated by a PI Controller. Subsequently, the DC power from the converter is transformed into AC power with the aid of 3φ VSI. Then, the PI controller is employed to regulate the function of the inverter, and the PWM generator is exploited to improve the functioning of the inverter. Furthermore, the obtained AC power is delivered to the 3φ grid with the aid of an LC filter, which provides harmonic less power to the grid.

2.1 PV system

Solar cells are semiconductors that generate Direct Current (DC) over PV panels by absorbing solar energy on frontal surfaces. As seen in Figure 2, the PV panel circuit is built with a diode, series resistance(R_S), a photocurrent(I_{ph}), and resistance that are connected in parallel (R_p) to indicate a current leakage.
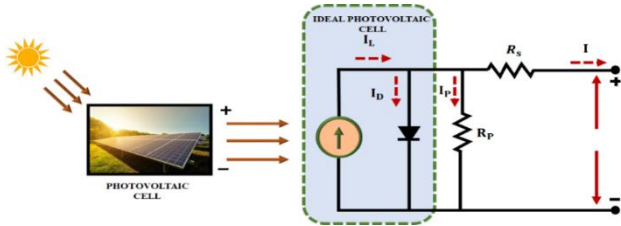
Figure 2. Circuit of PV system

By applying Kirchhoff's law, the current equation becomes,

$$I = I_{ph} - I_D - I_p \tag{1}$$

$$I_p = \frac{V + R_S I}{R_p} \tag{2}$$

The current via the diode is denoted as I_D and the magnitude of the diode current is denoted as,

$$I_D = I_{sd}\left(exp\left(\frac{q.(V+R_S.I)}{n.K.T}\right) - 1\right) \tag{3}$$

Where K stands for the Boltzmann constant and I_{sd} reverse saturation current. Climate circumstances cause the obtained PV voltage to decrease, so a converter is required to enhance the voltage to power the grid. The hybrid Boost-Cuk converter approach used in this work is explained in the following part.

2.2 Hybrid boost-cuk converter

The hybrid Boost-Cuk converter (Figure 3) integrates both Boost and Cuk converters to enhance the PV system's low voltage. The number of switches and diodes in a converter directly impacts its complex operation and control. Since each switch needs a gate drive signal to be controlled, this increase takes place. The developed converter has two stages of operation.

Stage 1:

When switch S is active at t_o, this stage is initiated (Figure 4). Considering that twice the input voltage is the same as the voltage across C_1 and input voltage is similar to V_{C2}. Then, half of the output voltage is the same as the voltage across C_3 and C_4. During this mode, the voltage across L_1 is positive. Consequently, the current flowing via the inductor is linearly increased.
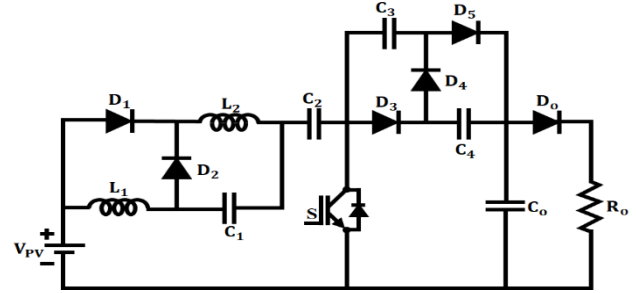
Figure 3. Hybrid boost-cuk converter

$$V_{L1} = V_{PV} + V_{C1} + V_{C2} \tag{4}$$

$$V_{C2}(t_o) = \frac{1}{2}V_{C1}(t_o) = V_{PV} \tag{5}$$

$$V_{L1} = 4V_{PV} \tag{6}$$

$$\Delta I_{L1} = \frac{4V_{PV}}{L_1}(t_1 - t_o) = \frac{4DV_{PV}}{L_1 f_s} \tag{7}$$

In this mode, the inductor L_1 receives energy from the input source and C_1 and C_2. The voltage across the inductor L_2 is,

$$V_{L2} = V_{PV} + V_{C2} = 2V_{PV} \tag{8}$$

$$\Delta I_{L2} = \frac{2V_{PV}}{L_2}(t_1 - t_0) = \frac{2DV_{PV}}{L_2 f_s} \tag{9}$$

Inductor L_2's current rises linearly as a result of the positive voltage across it. In this mode, L_2 receives energy from the input source and capacitor C_2.

$$V_{L3} = V_{PV} \tag{10}$$

$$\Delta I_{L3} = \frac{V_{PV}}{L_3}(t_1 - t_0) = \frac{V_{PV}D}{L_3 f_s} \tag{11}$$

$$\Delta I_{L1} = 2\Delta I_{L2} \tag{12}$$

$$t_1 - t_0 = DT \tag{13}$$

Where DT is the amount of time it takes for the switch to turn on and D is its duty cycle. A higher anode voltage activates a diode because diodes D_1 and D_2 share a cathode. Diode D_1's anode voltage is equal to V_{PV}, while diode D_2's anode voltage is equal to $-(V_{C1} + V_{C2})$. As a result, D_2 is reverse-biased. The voltage across the diode D_3 is calculated as follows because the switch is on.

$$V_{D3} = V_O - V_{C4} = \frac{V_O}{2} \tag{14}$$

Furthermore, diode D_5 is reverse-biased. In this mode, the output capacitor C_O is charging capacitors C_3 and C_4 and diode D_4 is forward-biased. However, the load is also delivered by the output capacitor. The nominal power determines the maximum input current in the developed converter. For a 100% efficiency assumption, the following expressions are obtained:

$$V_{O(max)} \times I_O = V_{in} \times I_{in(max)} \tag{15}$$

$$I_{in(max)} = \frac{V_{O(max)} \times I_O}{V_{in}} \tag{16}$$

$$V_{C3} + V_{C4} = V_O \tag{17}$$

As $C_3 = C_4$ and its voltage is half the output voltage.

Figure 4. Stages of developed converter

Figure 5. Switching the waveform of the converter

Stage 2:

When the switch is turned off at t_1, this mode is started. As a result, diode D_2 is forward-biased and diode D_1 is reversed-biased. Consequently, diodes D_2, D_3 and D_5 provide the necessary path to move the energy stored in inductors L_1 and L_2 to capacitors C_1 and C_2, and the output. The energy held in capacitors C_3 and C_4 is transferred to the load when diodes, D_3 and D_5 are turned on, while the diode D_4 is reverse-biased.

$$V_{L1} = V_{PV} + V_{C1} + V_{C2} + V_{C4} - V_O = 4V_{PV} - \frac{V_O}{2} \qquad (18)$$

Owing to the negative voltage through L_1, it's current reduces linearly

$$\Delta I_{L1} = \left(4V_{PV} - \frac{V_O}{2}\right) \times \frac{(t_2 - t_1)}{L_1} = \left(4V_S - \frac{V_O}{2}\right)\frac{(1-D)}{L_1 f_s} \qquad (19)$$

Based on the volt-second balance for the inductor L_1, the following expression is obtained:

$$4V_{PV}DT = \left(\frac{V_O}{2} - 4V_{PV}\right)(1-D)T \qquad (20)$$

When diode D_2 is active, the subsequent expressions are calculated,

$$V_{L2} = -V_{C1} = -2V_S \qquad (21)$$

$$\Delta I_{L2} = \frac{-2V_{PV}(1-D)}{L_2 f} \qquad (22)$$

In mode 2, capacitors C_3 and C_4 are connected in parallel,

$$V_{C3} = V_{C4} \qquad (23)$$

Figure 5 displays the switching waveform of the developed converter. After that, the PI controller is exploited to stabilize the voltage of the developed converter, and its parameters are tuned by the Bat-Chicken swarm optimization algorithm.

2.3 Bat-chicken swarm optimized PI controller

A Bat-Chicken swarm-optimized PI controller integrates the BA and CSO to tune the PI controller's parameters. This hybrid approach combines the exploration efficacy of BA and adaptive hierarchy-based dynamics of CSO to optimize the PI controller's performance. Figure 6 reveals the flowchart of the Bat-Chicken swarm-optimized PI controller. It initializes a population of potential solutions that represent distinct K_P and K_I pairs. BA highlights the phenomenon of echolocation by approaching the prey that has been identified, as bats search for it separately. This implies that a single random person is persuading the entire swarm to deviate in search of food.

Figure 6. Flowchart of Bat-Chicken swarm optimized PI controller

By shifting their current position, the entire swarm converges to the optimal solution across generations. The flight of a bat is:

$$Q_i^{(t)} = Q_{min}^{(t)} + \left(Q_{max}^{(t)} - Q_{min}^{(t)}\right) \cdot \beta \qquad (24)$$

$$V_i^{(t+1)} = V_i^{(t)} + \left[X_i^{(t)} - X_{best}^{(t)}\right] \cdot Q_i \qquad (25)$$

14

$$X_i^{(t+1)} = X_i^{(t)} + V_i^{(t)} \tag{26}$$

Where $X_i^{(t+1)}$ is the position of ith bat at generation, t, $V_i^{(t)}$ is the velocity of a single bat and $Q_i^{(t)}$ is the actual pulse frequency. Within the interval $Q_i^{(t)} \epsilon [Q_{min}, Q_{max}]$, the output pulse frequency is fluctuating. The output pulse is specified by the random number $\beta \in [0, 1]$, and the current best solution at the moment is shown by $X_{best}^{(t)}$. The two halves of the BA search process are exploitation and exploration. While exploitation guides the search in the vicinity of the current solutions, exploration refers to the discovery of new solutions. Since both processes usually rely on the variation operators, they can't be carried out concurrently. However, striking a balance between exploration and exploitation sets the control parameters. More ideal parameter configurations exist. Two exploration strategies and the parameter $r_i^{(t)}$ are used in the BA to balance the exploration and exploitation parts of the search process. The first exploration strategy is more exploratory in character, whereas the second method, which is given as:

$$X_{new} = X_{old} + \epsilon. \overline{A}^{(t)} \tag{27}$$

It employs the random walk, which is a type of local search that is more concerned with taking advantage of the best solution available at the moment. Let's observe that X_{old} in the equation displays the current best solution, whereas X_{new} presents the new best solution. $\overline{A}^{(t)}$ is the average loudness, while ϵ is the random number in the range $(-1,1)$. Chickens are a unique species of poultry animal due to their sociable character, and they usually work together to obtain food. Hens, chicks, and roosters are the three distinct groups of individuals that make up chicken flocks. Based on varying foraging hierarchies, the group exhibits a distinct foraging capacity. In this hierarchy, hens chase after roosters because they are better at foraging than they are, and chicks follow suit since they are less skilled at foraging.

The intelligent optimization algorithm's optimization object is the objective function that requires an optimal solution. Its independent variable parameters are composed of n j −dimensional space vectors X, where n is any positive integer, and j is the dimensionality. The Chicken Optimization Algorithm is divided into 3groups based on the number of vectors X. The first RN individuals with the lowest fitness value are assigned to the rooster group R_i; the Chick Group (CN) individuals with the highest fitness value are assigned to the chick group C_i; and the remaining Hen Group(HN) individuals are allocated to the hen group H_i. The corresponding numbers of individuals in each group within the colony are thus denoted by the letters Rooster Group (RN), HN, and CN.

$$R_i = \{R_1, R_2, \cdots, R_{RN}\} \tag{28}$$

$$C_i = \{C_1, C_2, \cdots, C_{CN}\} \tag{29}$$

$$H_i = \{H_1, H_2, \cdots, H_{HN}\} \tag{30}$$

The rooster group's location succession is:

$$R_{i,j}^{t+1} = R_{i,j}^t [1 + randn(0, \delta^2)] \tag{31}$$

$$\delta^2 = \begin{cases} 1, & f_i \le f_s \\ e^{\frac{f_s - f_i}{|f_i| + \epsilon}}, & f_i > f_s \\ S \epsilon [1, n], & s \ne i \end{cases} \tag{32}$$

Where $0, \delta^2$ is a Gaussian-distributed random number that obeys a 0 mean and variance of δ^2 and $R_{i,j}^t$ is the position of the ith rooster in the jth dimension following t iterations, the random rooster index, or S, is a small but significant integer that prevents the denominator from 0, while the individual's fitness value is denoted by f. The hen group's location succession is:

$$H_{i,j}^{t+1} = H_{i,j}^t + k_1 * rand * (R_{Hi}^t - M_{i,j}^t) + k_2 * rand * (RH^t - H_{i,j}^t) \tag{33}$$

$$k_1 = e^{\frac{f_{Hi} - f_{rHi}}{|f_{Hi}| + \epsilon}} \tag{34}$$

$$k_2 = e^{f_{RH} - f_{Hi}} \tag{35}$$

The position of the ith hen in the jth dimension following t iterations is denoted by $H_{i,j}^t$. A random number among 0 and 1 is called a rand. R_{Hi}^t is the position of the ith hen's leader rooster after t iterations; RH^t is the position of the randomly chosen individuals between the other roosters and hens, excluding the hen and leader cock, after t iterations; k_1 denotes the rooster's influence factor and k_2 represents the random individual effect factor. Where f_{Hi} represents the ith hen's fitness value. The rooster leading the hen has a fitness value of f_{rHi}. Where Eq. contains f_{RH}, the random person's fitness value. Location succession of the hen groups is:

$$C_{i,j}^{t+1} = C_{i,j}^t + F * (Hi_j^t - C_{i,j}^t) \tag{36}$$

The ith chick's position in the jth dimension after t iterations is denoted by $C_{i,j}^t$; the matching hen's position after t iterations is denoted by Hi_j^t; and F is a random number between 0 and 2.The hybrid algorithm iteratively refines K_p and K_i to minimize a fitness function defined by the control system's performance metrics. After reaching convergence, the best solution is selected as the optimized K_P and K_I values for the PI controller. This hybrid optimization approach is appropriate for complex and nonlinear systems, where traditional tuning methods are become infeasible because of dynamic variability or high dimensionality.

2.4 Battery

The battery is represented by the electrical circuit, shown in Figure 7. The electrolyte, plate grids, separator porosity, and connecting conductors develop the equivalent series resistance (R_B). The battery capacitance is represented by C_B, whereas the equivalent parallel resistance (R_p) is a representation of the impurities in the electrolyte and plates that cause the battery to gradually discharge when it is left disconnected (self- discharge resistance).
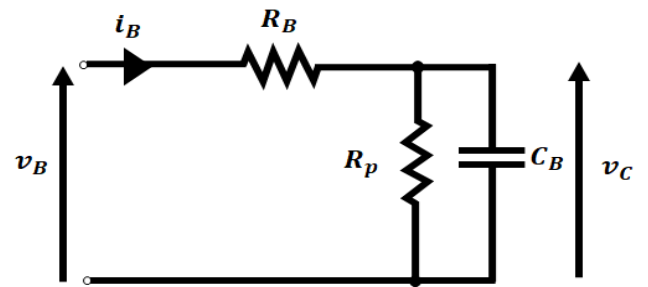
Figure 7. Circuit diagram of battery

Buck mode:

While the switch K_2 remains open($u_2 = 0$), the switch K_1 is controlled by a PWM signal $\{u_1 \epsilon\{0,1\}\}$ in this mode. After that, the DC bus transfers the electrical energy to the battery. The entire system (charger-battery) functions in G2V mode. However, the dc-dc converter functions in buck mode. Considering that u_1 is accept either 1 or 0, the subsequent switching model is derived:

$$L\frac{di_L}{dt} = -ri_L - v_B + u_1 V_{DC} \tag{37}$$

$$C\frac{dv_B}{dt} = i_L - \frac{1}{R_B}v_B + \frac{1}{R_B}v_C \tag{38}$$

$$C_B\frac{dv_C}{dt} = \frac{1}{R_B}v_B - \left(\frac{1}{R_B} + \frac{1}{R_p}\right)v_C \tag{39}$$

Boost mode:

In this mode, the switch K_1 remains open($u_1 = 0$), but only switch $K2$ is controlled by a PWM signal$\{u_2 \epsilon\{0,1\}\}$. After that, the battery transfers its electrical energy to the DC bus. While the entire system (charger-battery) functions in V2G mode, the DC-DC power converter functions in boost mode. Considering that u_2 accept either 1 or 0, the following switching model is derived.

$$L\frac{di_L}{dt} == -ri_L - v_B + (1 - \mu_2)V_{DC} \tag{40}$$

$$C\frac{dv_B}{dt} = i_L - \frac{1}{R_B}v_B + \frac{1}{R_B}v_c \tag{41}$$

$$C_B\frac{dv_C}{dt} = \frac{1}{R_B}v_B - \left(\frac{1}{R_B} + \frac{1}{R_p}\right)v_C \tag{42}$$

Then, the output of the converter is fed into the VSI that transforms the DC to AC voltage, and grid synchronization is discussed below.

2.5 3ϕ Grid Synchronization

A passive Low-pass filter (LPF) filters the output voltage of a controlled VSI, as shown in Figure 8. At the point of common coupling, the filtered voltage that is almost harmonic-free is synchronized with the grid voltage. The connection is guaranteed by the coupling breaker. The filtered VSI and grid voltage are converted into the inverter's rotating orthogonal frame. It is presumed that the inverter's frame and the reference signal frame are arranged so that the inverter's quadrature component,U_{qinv} denotes its magnitude and its direct component, U_{dinv}, equals zero. Since U_{qf} and U_{qg} stand for the quadrature components, U_{df} and U_{dg} are the filtered inverter voltage and the grid voltage's direct components. Because of this arrangement, the direct components are ideal indicators of the phase shift among the inverter reference signal and the filtered and grid voltages. The initial and preliminary stage of synchronization is accomplished by regulating the inverter voltage to match the grid's magnitude. The phase-angle matching procedure is the second and most important stage. Where U_f and U_g are the inverter-filtered and grid voltage magnitudes, respectively, The inverter reference signal's phase angle is represented byθ_{inv}, the filtered VSI voltage by θ_f and the grid voltage by θ_g.

$$U_{df} = -\widehat{U_f}sin(\theta_{inv} - \theta_f) \tag{43}$$

$$U_{dg} = -\widehat{U_g}sin(\theta_{inv} - \theta_g) \tag{44}$$

$$U_{qf} = -\widehat{U_f}cos(\theta_{inv} - \theta_f) \tag{45}$$

$$U_{qg} = -\widehat{U_g}cos(\theta_{inv} - \theta_g) \tag{46}$$
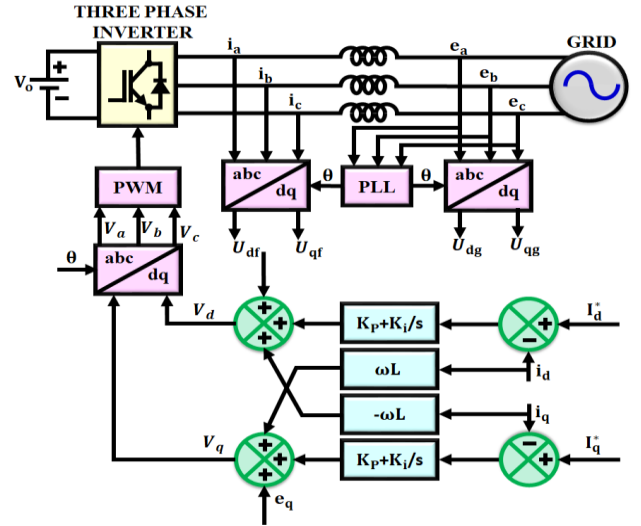
Figure 8. Grid synchronization

Utilizing the phase-shift representative value, the inverter frequency is adjusted to ensure that the grid and the inverter direct components are identical to achieve a zero phase-shift among the voltages.

$$e_\theta = \left(U_{df} \times U_{qg} - U_{qf} \times U_{dg}\right) \tag{47}$$

$$e_\theta = \widehat{U_f}.\widehat{U_g}sin(\theta_f - \theta_g) \tag{48}$$

When the voltage of the grid θ_g and the VSI voltage phase-angle θ_f are equal, leading the equation (48) to be zero. While both voltage magnitudes are identical, this results in $U_{df} = U_{dg}$.

$$e_\theta = \widehat{U_f}.\widehat{U_g}(\theta_f - \theta_g) \tag{49}$$

This is the same as the SRF-PLL's controlled voltage value. The distinction is that, in this case, the phase shift is calculated between two measured voltages that need to be synchronized rather than between a measured signal and the internal PLL frame. To guarantee a zero phase-shift among the voltages, the value is regulated to zero is denoted by e_θ. Since the phase control is solely reliant on the constancy of the voltage magnitudes, it is crucial to begin controlling the voltage magnitude before controlling the phase. Since the phase control is based on actual voltage levels, any disruption brought on by the magnitude control has a significant impact on it.

3. Results and discussion

This part analyzes the outcomes of a developed PV-based grid system using MATLAB/Simulink software. It also includes a comparison of conventional approaches with developed work. Table 1 displays the parameters of the developed research.

Case 1: Constant temperature and intensity

Figure 9 represents the characteristics of solar panels in constant temperature and intensity conditions. The temperature is sustained at a stable value of 35 ℃ without distortions. Also, the intensity value of solar panels is sustained to a value of 1000(W/(Sq.m)) without any fluctuations. Subsequently, the voltage of the solar panel is stabilized at a stable value of 310 V throughout the system. Likewise, the current of the solar panel gradually decreased

in the starting stage, and it maintained a value of 50 A in the entire system.

Table 1. Parameters of developed work

Parameter	Specification
PV System	
Rated Power	10kW
No. of Panels in Parallel	3
Open Circuit Voltage	37.25V
Cell linked in Series	36
No. of Panels in series	12
Short Circuit Current	8.95A
Hybrid Boost-Cuk Converter	
C_1, C_2, C_3 and C_4	22 μF
Switching frequency	10KHz
L_1, L_2	4.7mH
C_O	2200μF
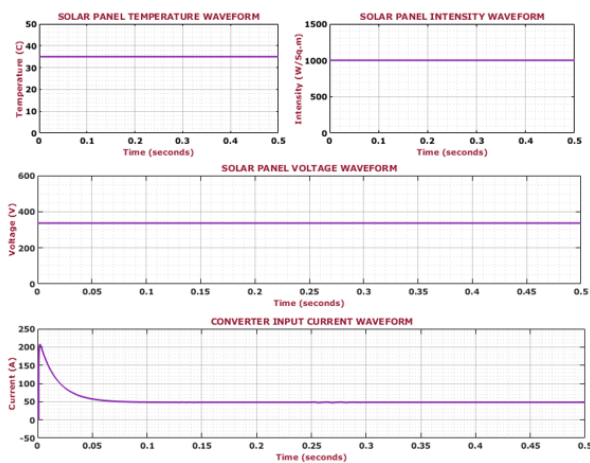
Figure 9. Characteristics of solar panel

Figure 10 displays the developed converter's waveform. The output voltage of the developed converter is linearly changed in the initial period, and it stabilizes at 600 V with the aid of the BCSO-PI controller. In the initial period, the output current slowly varied, and then it was sustained at a value of 24 A with little distortions. Figure 11 reveals the battery's waveform. The battery's State of Charge (SOC)value is maintained at a stable 80 % throughout the system. The battery voltage is sustained at 50V without any oscillations. Consequently, the battery current is maintained at a constant 2A with few fluctuations. Figure 12 illustrates the grid waveform. The grid voltage is stabilized at a constant value of 420 V without any fluctuations. Likewise, the grid current is maintained at a stable value of 12 A throughout the system. The Real power waveform remains stable at approximately 8000 W, indicating steady energy consumption or generation. Meanwhile, the reactive power waveform is constant at around 600 VAR, reflecting steady reactive power demand, as seen in Figure 13.

Case 2: Varying temperature and intensity

Figure 14 represents the characteristics of solar panels in varying temperatures and irradiation conditions. Initially, the solar panel's temperature is varied, and it is stabilized at a value of 35 °C without any fluctuations. Similarly, the intensity of the solar panel is changed, and it maintains a constant value of 1000(W/(Sq.m))in the entire system. Likewise, the solar panel voltage is changed and sustained at a stable value of

310V without any oscillations. Initially, the input current is randomly varied and gets sustained at a stable value of 50 A.
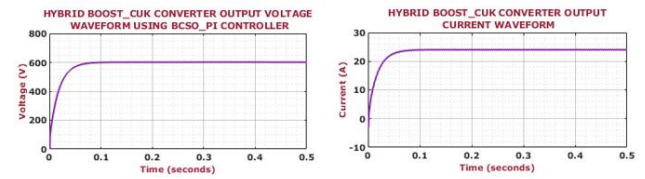
Figure 10. Waveform of the developed converter with BCSO-PI controller
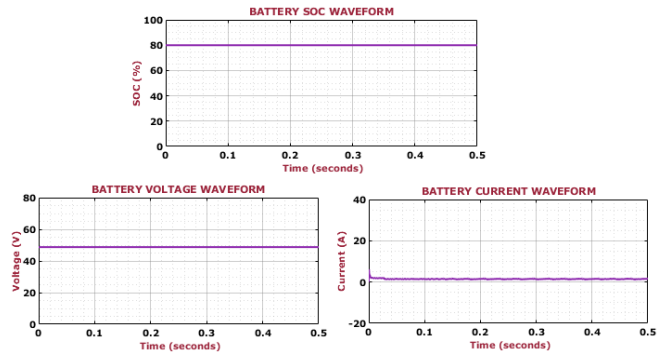
Figure 11. Waveform of battery
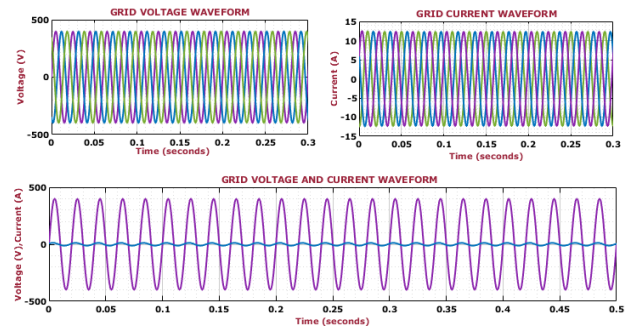
Figure 12. Waveform of grid
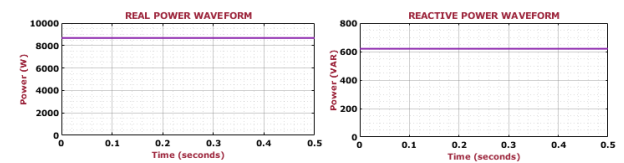
Figure 13. The waveform of real and reactive power

The waveform of the developed converter with the BCSO-PI controller is revealed in Figure 15. At the starting stage, the output voltage is linearly changed, and it is increased to a stable value of 600 V. Consequently, the output current is gradually raised and settled to a value of 24A without distortions.

The R phase's THD value of 0.58% is within acceptable limits, representing a high-quality power signal with negligible harmonic interference. Also, the Y phase (0.68%) has slightly higher harmonic distortion than the R phase. Subsequently, the B phase has the lowest THD of 0.51%

among the three phases, indicating a smoother power signal, as seen in Figure 16.
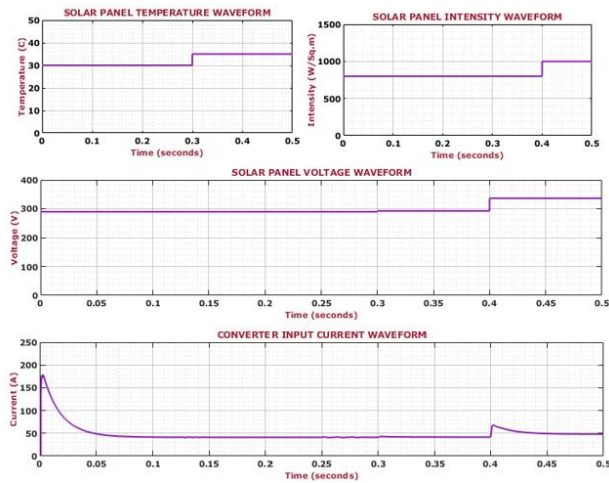
Figure 14. Characteristics of solar panel
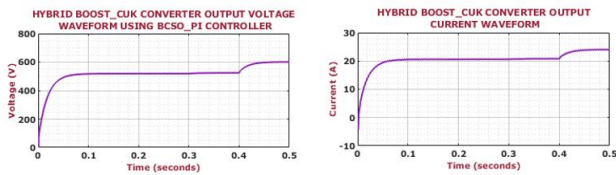
Figure 15. Waveform of the developed converter with BCSO-PI controller

Figure 17 illustrates an analysis of efficiency for four different converters: Buck-Boost [24], High Gain Cuk [25], Z Source Boost [26], and the developed converter. The proposed converter attains the highest efficiency at 93%, highlighting its superior performance compared to the other converters. This makes it a promising choice for applications requiring high efficiency in power conversion. A comparative analysis of converter performance in terms of switching loss, inductor loss, capacitor loss, and diode loss for interleaved step-down converter [27] and Hybrid Boost-Cuk converter is displayed in Figure18. The Interleaved Step-Down Converter suffers more from inductor losses, making it less efficient in handling energy conversion. The Hybrid Boost-Cuk Converter demonstrates improvements in reducing inductor losses but experiences higher diode losses. Figure 19 shows the voltage gain for three types of converters: Transformerless [28], Interleaved Bi-directional [29], and the developed converter. The transformerless converter attains the highest voltage gain at all duty ratios, demonstrating superior performance in boosting voltage. The Interleaved Bi-directional Converter offers a balanced performance, providing moderate voltage gain. The Proposed Converter prioritizes other design objectives, such as reduced complexity, cost, or improved efficiency in specific operational conditions, over-achieving maximum voltage gain. Figure 20 depicts a comparative analysis of control approaches based on settling time and rise time for GWO-PI, Modified LOA-PI, and proposed PI controller. The BAT-CSO PI approach is the most efficient control method, achieving both the shortest settling time of 0.023 s and a rise time of 0.021 s. The BAT-CSO PI approach offers a balanced performance with results that are not as fast as GWO-PI [30] but considerably better than Modified LOA-PI [31].
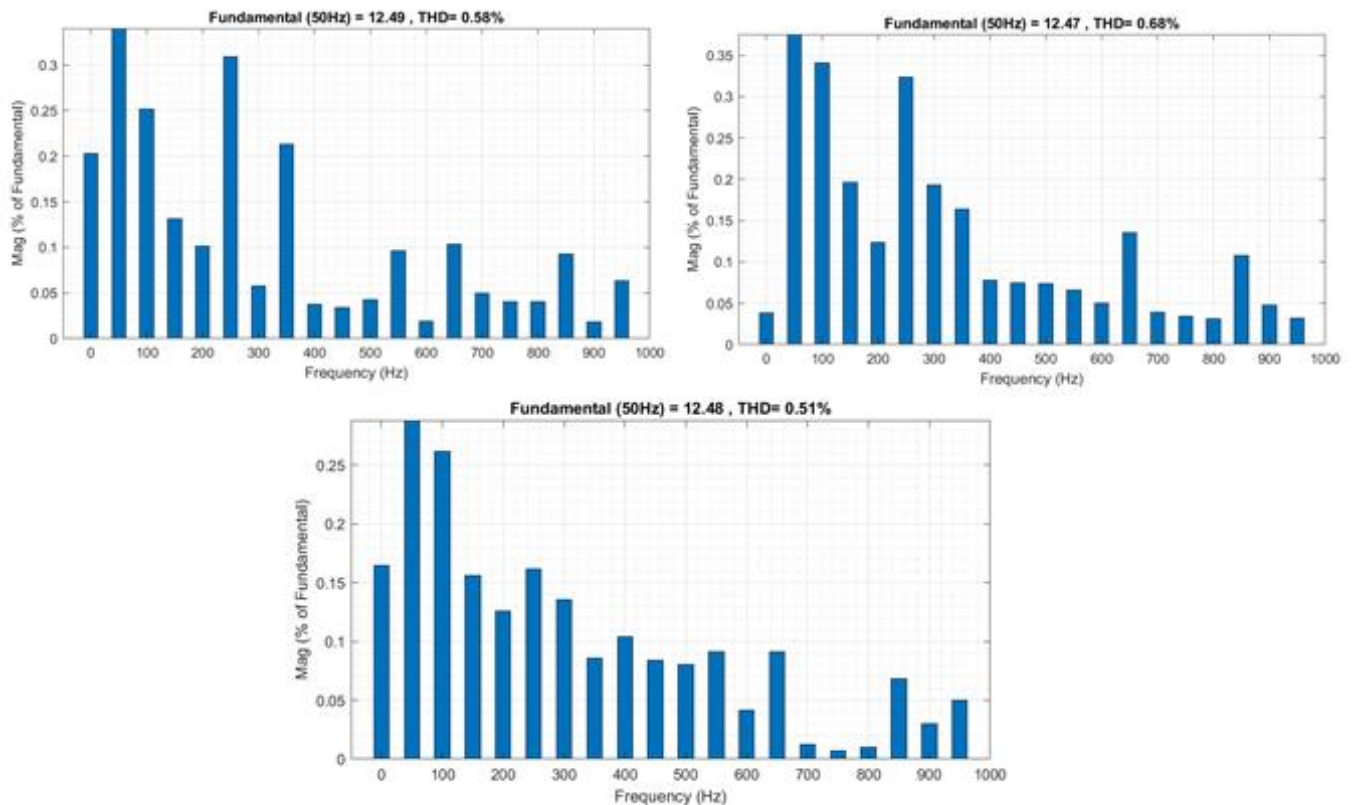
Figure 16. Waveform of THD
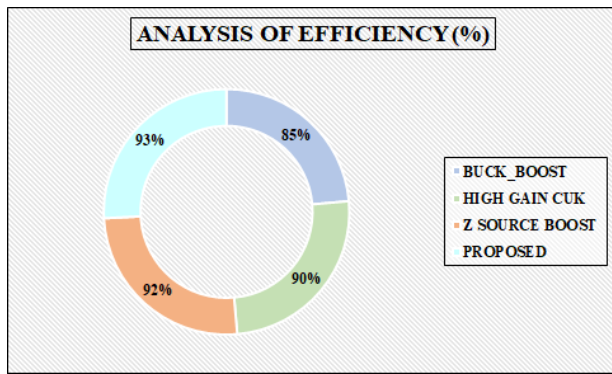
Figure 17. Analysis of efficiency
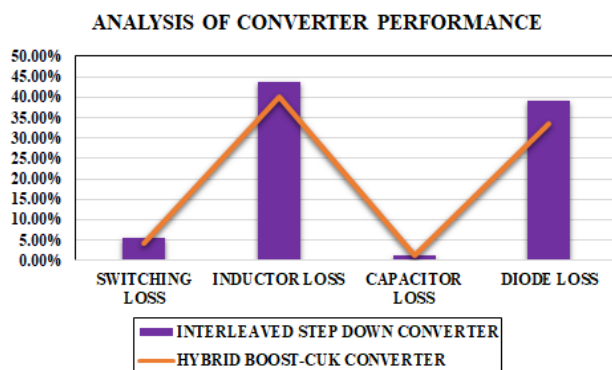
Figure18. Analysis of converter performance
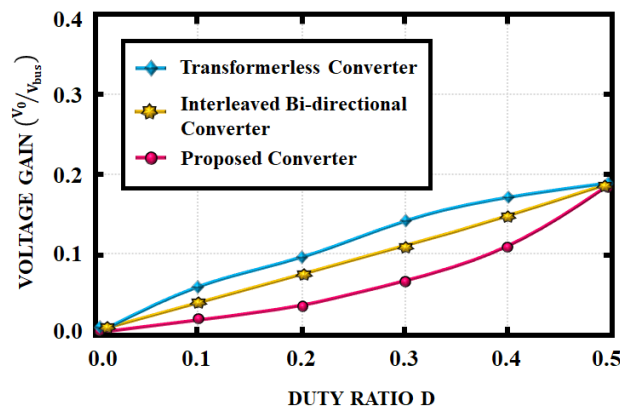
Figure 19. Analysis of voltage gain
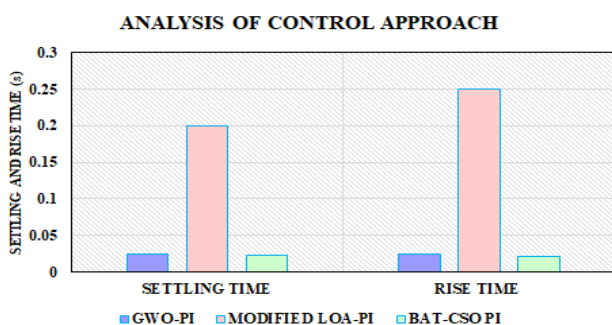
Figure 20. Analysis of the control approach

4. Conclusion

This research presents the importance of a PV-based hybrid Boost-Cuk converter for an efficient energy generation process. The hybrid Boost-Cuk converter linked to the PV system's output side increases output voltage while lowering switching loss. With less iteration before convergence, the applied Bat-Chicken swarm-optimized PI controller yields a higher gain, providing better control performance. Additionally, a steady power supply is guaranteed by the BESS, which is connected to the microgrid via a battery converter that ensures grid stability by supplying extra energy to the grid during periods of peak demand. Finally, the obtained DC supply harnessing 3ϕ VSI transforms the DC supply to AC, resulting in effective grid synchronization. The system's dependability and effectiveness are confirmed by the MATLAB/Simulink tool, which shows an efficiency of 93 % with maximum voltage gain.

Ethical issue
The authors are aware of and comply with best practices in publication ethics, specifically with regard to authorship (avoidance of guest authorship), dual submission, manipulation of figures, competing interests, and compliance with policies on research ethics. The authors adhere to publication requirements that the submitted work is original and has not been published elsewhere.

Data availability statement
The manuscript contains all the data. However, more data will be available upon request from the authors.

Conflict of interest
The authors declare no potential conflict of interest.

References
[1] M. Liaqat, M. G. Khan, M. R. Fazal, Y. Ghadi and M. Adnan, "Multi-Criteria Storage Selection Model for Grid-Connected Photovoltaics Systems," in IEEE Access, vol. 9, pp. 115506-115522, 2021.https://doi.org/10.1109/ACCESS.2021.3105592

[2] A. Laib, A. Krama, A. Sahli, A. Kihal and H. Abu-Rub, "Reconfigurable Model Predictive Control for Grid Connected PV Systems Using Thirteen-Level Packed E-Cell Inverter," in IEEE Access, vol. 10, pp. 102210-102222, 2022.https://doi.org/10.1109/ACCESS.2022.3208106

[3] W. Dong, H. Diao, J. Xu, J. Kang and Z. Lv, "Analysis and Parameters Design of Grid-Forming Converter for Enhancing the Stability of Photovoltaic Storage System Under Weak Grid," in IEEE Access, vol. 12, pp. 134273-134284, 2024. https://doi.org/10.1109/ACCESS.2024.3449340

[4] A. Almarshoud, "A techno-economic investigation for utilizing solar energy in irrigation of palm trees in Saudi Arabia," Future Sustainability, vol. 2, no. 1, pp. 35-46, 2022. https://doi.org/10.55670/fpll.fusus.2.1.4

[5] Y. Kassem, H. Gökçekuş and Q. A. Furaiji, "Applicability of solar systems with various technologies and sun-tracking: A case study of Baghdad, Iraq," Future Energy, vol. 1, no. 2, pp. 03-08, 2022. https://doi.org/10.55670/fpll.fuen.1.2.2

[6] F. Wu, B. Yang, A. Hu, Y. Zhang, W. Ge, L. Ni, C. Wang and Y. Zha, "Inertia and Damping Analysis of Grid-Tied Photovoltaic Power Generation System With DC Voltage Droop Control," in IEEE Access, vol. 9, pp.

38411-38418,
2021.https://doi.org/10.1109/ACCESS.2021.3059687

[7] C. Subramani, K. Dhineshkumar and P. Palanivel, "Design and implementation of 13 levels multilevel inverter for photovoltaic system," In Journal of Physics: Conference Series, vol. 1000, no. 1, pp. 012047. IOP Publishing, 2018.

[8] I. Hassan, I. Alhamrouni, Z. Younes, N. H. Azhan, S. Mekhilef, M. Seyedmahmoudian and A. Stojcevski, "Explainable Deep Learning Model for Grid-Connected Photovoltaic System Performance Assessment for Improving System Reliability," in IEEE Access, vol. 12, pp. 120729-120746, 2024.https://doi.org/10.1109/ACCESS.2024.3452778

[9] J. Luo, K. Panchabikesan, K. Lai, T. O. Olawumi, M. C. Mewomo, Z. Liu, "Game-theoretic optimization strategy for maximizing profits to both end-users and suppliers in building rooftop PV-based microgrids," Energy, vol. 313, pp.133715, 2024.https://doi.org/10.1016/j.energy.2024.133715

[10] K. S. Kavin, P. S. Karuvelam, M. Matcha and S. Vendoti, "Improved BRBFNN-based MPPT algorithm for coupled inductor KSK converter for sustainable PV system applications," Electrical Engineering, pp. 1-23. 2025. https://doi.org/10.1007/s00202-025-02952-9

[11] K. P. Joshua, L. V. Rangasamy, C. V. Reddy and R. Veeruchinnan, "Energy management of solar photovoltaic fed water pumping system based BLDC motor drive using NBO–SDRN approach," Electrical Engineering, vol. 106, no. 3, pp. 3045-3059, 2024.https://doi.org/10.1007/s00202-023-02102-z

[12] Q. Zhong, Y. Qiu, Y. Zhao, H. Li, G. Wang and F. Wen, "Interharmonic Analysis Model of Photovoltaic Grid-connected System with Extended Dynamic Phasors," in Journal of Modern Power Systems and Clean Energy, vol. 9, no. 6, pp. 1540-1547, 2021.https://doi.org/10.35833/MPCE.2020.000241

[13] S. M. Said, M. Aly and H. Balint, "An Efficient Reactive Power Dispatch Method for Hybrid Photovoltaic and Superconducting Magnetic Energy Storage Inverters in Utility Grids," in IEEE Access, vol. 8, pp. 183708-183721, 2020. https://doi.org/10.1109/ACCESS.2020.3029326

[14] K. S. Kavin, P. Subha Karuvelam, M. Devesh Raj and M. Sivasubramanian, "A Novel KSK Converter with Machine Learning MPPT for PV Applications," Electric Power Components and Systems, pp. 1-19, 2024.https://doi.org/10.1080/15325008.2024.2346806

[15] S. Chitra Selvi, R. Govindaraj, S. Chowdhury, S. Singh and B. Khan, "Embedded-Based Quadratic Boost Converter With Sliding-Mode Controller for the Integration of Solar Photo-Voltaic Source With Microgrid," in IEEE Journal of the Electron Devices Society, vol. 12, pp. 831-841, 2024.https://doi.org/10.1109/JEDS.2023.3340249

[16] N. A. Ahmed, B. N. Alajmi, I. Abdelsalam and M. I. Marei, "Soft Switching Multiphase Interleaved Boost Converter With High Voltage Gain for EV Applications," in IEEE Access, vol. 10, pp. 27698-27716, 2022. https://doi.org/10.1109/ACCESS.2022.3157050

[17] H. Y. Ahmed, O. Abdel-Rahim and Z. M. Ali, "New high-gain transformerless dc/dc boost converter system," Electronics, vol. 11, no. 5, pp. 734, 2022.https://doi.org/10.3390/electronics11050734

[18] Z. Haider, A. Ulasyar, A. Khattak, H. S. Zad, A. Mohammad, A. A. Alahmadi and N. Ullah, "Development and analysis of a novel high-gain CUK converter using voltage-multiplier units," Electronics, vol. 11, no. 17, pp. 2766, 2022.https://doi.org/10.3390/electronics11172766

[19] H. Gholizadeh and S. Hasanpour, "A New Quadratic CUK-Based Step-Up DC/DC Converterwithout Right Hand Plane Zero," International Journal of Industrial Electronics Control and Optimization, vol. 8, no. 1, pp.25-35, 2025.https://doi.org/10.22111/ieco.2024.48683.1565

[20] M. H. Demir and M. Demirok, "Designs of particle-swarm-optimization-based intelligent PID controllers and DC/DC Buck converters for PEM fuel-cell-powered four-wheeled automated guided vehicle," Applied Sciences, vol. 13, no. 5, pp. 2919, 2023.https://doi.org/10.3390/app13052919

[21] M. Shamseldin, M. A. Ghany and Y. Hendawey, "Optimal nonlinear PID speed control based on harmony search for an electric vehicle," Future Engineering Journal 2, no. 1, pp.4, 2021.

[22] C. Esakkiappan, "Soft Computing Based Tuning of PI Controller With Cuckoo Search Optimization For Level Control of Hopper Tank System," 2021.https://doi.org/10.21203/rs.3.rs-920228/v1

[23] L. Amador-Angulo, O. Castillo, C. Peraza and P. Ochoa,"An efficient chicken search optimization algorithm for the optimal design of fuzzy controllers," Axioms, vol. 10, no. 1, pp. 30, 2021.https://doi.org/10.3390/axioms10010030

[24] S. Saravanan, P. Usha Rani and M. P. Thakre, "Evaluation and Improvement of a Transformerless High-Efficiency DC–DC Converter for Renewable Energy Applications Employing a Fuzzy Logic Controller," Mapan - Journal of Metrology Society of India, vol. 37, no. 2, pp. 291–310, 2022, https://doi.org/10.1007/s12647-021-00530-5

[25] Z. Haider, A. Ulasyar, A. Khattak, H. S. Zad, A. Mohammad, A. A. Alahmadi and N. Ullah, "Development and analysis of a novel high-gain CUK converter using voltage-multiplier units," Electronics, vol. 11, no. 17, pp.2766, 2022.https://doi.org/10.3390/electronics11172766

[26] M. Saranya and G.G. Samuel, "Energy management in hybrid photovoltaic–wind system using optimized neural network," Electr Eng, vol. 106, pp. 475–492, 2024. https://doi.org/10.1007/s00202-023-01991-4

[27] C. L. Shen, P. H. Chen, H. Q. Liu, Y. S. Liang, "Interleaved step-down converter with capacitor-diode voltage splitter and minimum switches for low current ripple and extra-low voltage ratio," Discover Applied Sciences, vol. 6, no. 6, pp. 293, 2024.https://doi.org/10.1007/s42452-024-05987-y

[28] L. Yu, L. Wang, C. Yang and M. Wu, "Analysis and implementation of a single-stage transformer-less converter with high step-down voltage gain for voltage

regulator modules, IEEE Trans Ind Electron, vol. 68, no. 12, pp. 12239–49, 2021. https://doi.org/10.1109/TIE.2020.3045592

[29] Y. Zhang, W. Zhang, F. Gao, S. Gao and D. J. Rogers, "A switched-capacitor interleaved bidirectional converter with wide voltage-gain range for super capacitors in EVs. IEEE Trans Power Electron, vol. 35, no. 2, pp. 1536–47, 2020. https://doi.org/10.1109/TPEL.2019.2921585

[30] G. Vasumathi, V. Jayalakshmi and K. Sakthivel, "Efficiency analysis of grid tied PV system with KY integrated SEPIC converter," Measurement: Sensors, vol. 27, pp. 100767, 2023.https://doi.org/10.1016/j.measen.2023.100767

[31] R. Ramani and A. Nalini, "Enhanced EV Battery Monitoring Using IoT with Improved SEPIC-ZETA Converter and Modified Lion Optimization for Photovoltaic Systems," Journal of Electrical Systems, vol. 20, no. 6s, pp. 3005-3018, 2024.